Efficient Hyper-parameter Search for Knowledge Graph Embedding

Anonymous ACL submission

Abstract

While hyper-parameters (HPs) are important for knowledge graph (KG) embedding, existing methods fail to search them efficiently. To solve this problem, we first analyze the properties of different HPs and quantize the transferability from small subgraph to the large graph. Based on the analysis, we propose an efficient two-stage search algorithm, which efficiently explores HP configurations on small subgraph at the first stage and transfers the top configurations for fine-tuning on the large whole graph at the second stage. Experiments show that our method can consistently find better HPs than the baseline algorithms with the same time budget. We achieve 10.8% average relative improvement for four embedding models on the large-scale KGs in open graph benchmark.

1 Introduction

Knowledge graph (KG) is a special kind of graph structured data to represent knowledge through entities and relations between them (Wang et al., 2017; Ji et al., 2021). KG embedding, which encodes entities and relations as low dimensional vectors, is important for learning from KGs (Wang et al., 2017; Ji et al., 2021). The existing models range from translational distance models (Bordes et al., 2013), tensor factorization models (Nickel et al., 2011; Trouillon et al., 2017; Balažević et al., 2019), neural network models (Dettmers et al., 2017; Guo et al., 2019), to graph neural networks (Schlichtkrull et al., 2018; Vashishth et al., 2020).

Hyper-parameter (HP) search (Claesen and De Moor, 2015) is very essential when applying KG embedding. As studied, the HP configurations greatly influence the model performance (Ruffinelli et al., 2019; Ali et al., 2020). An appropriate HP configuration can help us make a more scientific understanding of the contributions made by existing works (Rossi et al., 2021; Sun et al., 2020). It is also important when adopting KG embedding methods to the real-world applications (Bordes et al., 2014; Zhang et al., 2016; Saxena et al., 2020).

Algorithms for HP search on general machine learning problems have been well-developed (Claesen and De Moor, 2015). As in Figure 1(a), the search algorithm selects a HP configuration from the search space in each iteration, then the evaluation feedback obtained by full model training is used to update the search algorithm. The optimal HP is the one achieving the best performance on validation data in the search process. Representative algorithms are within sample-based methods like grid search, random search (Bergstra and Bengio, 2012), and sequential model-based Bayesian optimization (SMBO) methods like Hyperopt (Bergstra et al., 2013), SMAC (Hutter et al., 2011), Spearmint (Snoek et al., 2012), and BORE (Tiao et al., 2021), etc. Recently, there rises some subgraph-based methods (Tu et al., 2019; Wang et al., 2021) which learn a surrogate model with configurations efficiently evaluated on small subgraphs, and transfer the model to guide HP search on the whole graph. However, these methods fail to search a good configuration of HPs for KG embedding models in limited time since there lacks the understanding on the influence and correlation of the HPs, and they do not well explore the transferability from small subgraph to the whole graph.

To address the limitations of conventional HP search algorithms, we give a comprehensive understanding on the influence and correlation of HPs and their transferability from small subgraph to the large whole graph in KG embedding. By analyzing the ranking distribution of each HP value, we reduce the range of HP values that are not good in most cases. We observe that the choices of batch size and dimension size do not influence much on the ranking of the other HPs. Hence, small batch size and dimension size with lower time cost can achieve more efficient evaluation. Besides, transferring evaluations on a subgraph is highly correlated

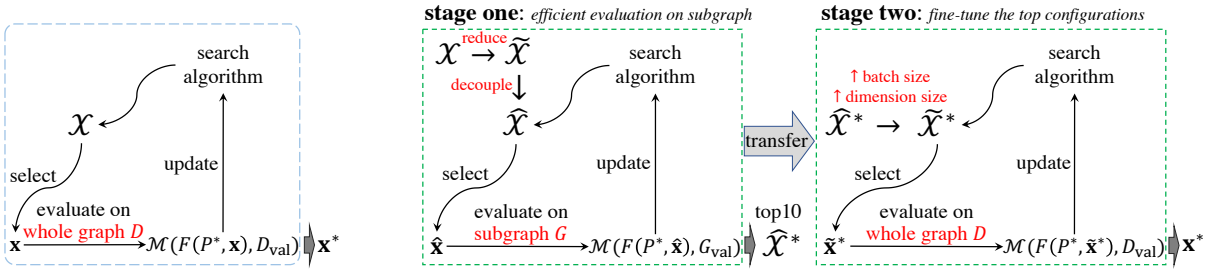

(a) Conventional methods. (b) TOSS.

Figure 1: The framework of conventional HP search algorithm and the proposed TOSS.

with the evaluations on the whole graph.

The understanding motivates us to reduce the size of search space, and design a *T*w*O*-*S*tage *S*earch algorithm, named TOSS. As in Figure 1(b), TOSS efficiently explores HP configurations in the decoupled space with the algorithm RF+BORE (Tiao et al., 2021) on a subgraph in the first stage. Then in the second stage, the top configurations are equipped with large batch size and dimension size for fine-tuning on the whole graph.

With the same time budget, TOSS can consistently search better configurations than the baseline search algorithms for seven embedding models on WN18RR and FB15k-237. By applying TOSS to the large-scale benchmarks ogbl-biokg and ogbl-wikikg2, the performances of embedding models are improved compared with the reported results on OGB link prediction board. Besides, we use ablation studies to analyze the design components in TOSS to justify the efficiency improvement.

2 Background: HPs in KG embedding

We firstly revisit the important and common HPs in KG embedding. Following the general frameworks (Ruffinelli et al., 2019; Ali et al., 2020), the learning problem can be simplified as

$$\boldsymbol{P}^* = \arg\min_{\boldsymbol{P}} L(F(\cdot, \boldsymbol{P}), D^+_{\text{tra}}, D^-) + r(\boldsymbol{P}), \quad (1)$$

where F is the form of embedding model with parameters $\boldsymbol{P}$, D^+_{tra} is the training data, D^- represents negative samples, and $r(\cdot)$ is a regularization function. There are four groups of hyper-parameters (Table 1), i.e., the size of *negative sampling* for D^-, the choice of *loss function* L, the form of *regularization* $r(\cdot)$, and the *optimization* $\arg\min_{\boldsymbol{P}}$.

Embedding model. There are many embedding models in the literature. We follow (Ruffinelli et al., 2019) to focus on some representative models. They are translational distance models TransE (Bordes et al., 2013) and RotatE (Sun et al., 2019), tensor factorization models RESCAL (Nickel et al., 2011), DistMult (Yang et al., 2015), ComplEx (Trouillon et al., 2017) and TuckER (Balažević et al., 2019), and neural network models ConvE (Dettmers et al., 2017). Graph neural networks for KG embedding (Schlichtkrull et al., 2018; Vashishth et al., 2020) are not studied for their scalability issues on large-scale KGs (Ji et al., 2021).

Negative sampling. Sampling negative triplets is important as only positive triplets are contained in the KGs (Wang et al., 2017). We can pick up m triplets by replacing the head or tail entity with uniform sampling (Bordes et al., 2013) or use a full set of negative triplets. Using the full set can be defined as the 1VsAll (Lacroix et al., 2018) or kVsAll (Dettmers et al., 2017) according to the positive triplets used. The methods (Cai and Wang, 2018; Zhang et al., 2021) requiring additional models for negative sampling are not considered here.

Loss function. There are three types of loss functions. One can use margin ranking (MR) loss (Bordes et al., 2013) to rank the positive triplets higher over negative triplets, or use binary cross entropy (BCE) loss, with variants BCE_mean, BCE_adv (Sun et al., 2019), and BCE_sum (Trouillon et al., 2017), to classify the positive and negative triplets as binary classes, or use cross entropy (CE) loss (Lacroix et al., 2018) to classify the positive triplet as the true label over the negative triplets.

Regularization. To balance the model expressiveness and complexity, and to avoid unbounded embedding, the regularization techniques can be considered, such as regularizers like Frobenius norm (FRO) (Yang et al., 2015; Trouillon et al., 2017), Nuclear norm (NUC) (Lacroix et al., 2018) as well as DURA (Zhang et al., 2020), and dropout on the embeddings (Dettmers et al., 2017).

Optimization. To optimize the embeddings, important optimization choices include the optimizer, such as SGD, Adam (Kingma and Ba, 2014) and Adagrad (Duchi et al., 2011), learning rate, initializers, batch size, embedding dimension size, and add inverse relation (Lacroix et al., 2018) or not.

Table 1: The ranges of HPs. Conditioned HPs are in parenthesize. "adv." and "reg." is short for "adversarial" and "regularization", respectively. Please refer to the Appendix A for more details.

component	name	type	range
negative sampling	# negative samples	cat	{32, 128, 512, 2048, 1VsAll, kVsAll}
loss function	loss function	cat	{MR, BCE_(mean, sum, adv), CE}
	gamma (MR)	float	[1, 24]
	adv. weight (BCE_adv)	float	[0.5, 2.0]
regularization	regularizer	cat	{FRO, NUC, DURA, None}
	reg. weight (not None)	float	$[10^{-12}, 10^{2}]$
	dropout rate	float	$[0, 0.5]$
optimization	optimizer	cat	{Adam, Adagrad, SGD}
	learning rate	float	$[10^{-5}, 10^{0}]$
	initializer	cat	{uniform, normal, xavier_uniform, xavier_norm}
	batch size	int	{128, 256, 512, 1024}
	dimension size	int	{100, 200, 500, 1000, 2000}
	inverse relation	bool	{True, False}

3 The search problem

An instance $\mathbf{x} = (x_1, x_2 \ldots, x_n)$ in the search space $\mathcal{X}$ is called a HP configuration. Let $F(\boldsymbol{P}, \mathbf{x})$ be an embedding model with model parameters $\boldsymbol{P}$ and HPs $\mathbf{x}$, we define $\mathcal{M}(F(\boldsymbol{P}, \mathbf{x}), D_{\text{val}})$ as the performance measurement (the larger the better) on validation data D_{val} and $\mathcal{L}(F(\boldsymbol{P}, \mathbf{x}), D_{\text{tra}})$ as the loss function (the smaller the better) on training data D_{tra}. We define the problem of HP search for KG embedding models in Definition 1. The objective is to search an optimal configuration $\mathbf{x}^* \in \mathcal{X}$ such that the embedding model F can achieve the best performance on the validation data D_{val}.

Definition 1 (Hyper-parameter search for KG embedding)**.** *The problem of HP search for KG embedding model is formulated as*

$$\mathbf{x}^* = \arg\max_{\mathbf{x}\in\mathcal{X}} \mathcal{M}\big(F(\boldsymbol{P}^*, \mathbf{x}), D_{val}\big), \quad (2)$$

$$\boldsymbol{P}^* = \arg\min_{\boldsymbol{P}} \mathcal{L}\big(F(\boldsymbol{P}, \mathbf{x}), D_{tra}\big). \quad (3)$$

Definition 1 is a bilevel optimization problem (Colson et al., 2007), which can be solved by many conventional HP search algorithms. The most common and widely used approaches are sample based methods like grid search and random search (Bergstra and Bengio, 2012), where the HP configurations are independently sampled. To guide the sampling of HP configurations, SMBO-based methods (Bergstra et al., 2011; Hutter et al., 2011) learn a surrogate model to select configurations based on the predicted results. Then, the parameters $\boldsymbol{P}$ are optimized by minimizing the loss function $\mathcal{L}$ on D_{tra} in (3). The evaluation feedback $\mathcal{M}$ of $\mathbf{x}$ on the validation data D_{val} is used to update the surrogate.

There are three major aspects determining the efficiency of Definition 1: (i) the size of search space $\mathcal{X}$, (ii) the validation curvature of $\mathcal{M}(\cdot, \cdot)$ in (2), and (iii) the evaluation cost in solving $\arg\min_{\boldsymbol{P}} \mathcal{L}$ in (3). However, the existing HP search methods directly search on a huge space with commonly used surrogate models and slow evaluation feedback from the whole KG. They lack the understanding on the search problem, and fail to efficiently find good HP configurations.

4 Understanding the search problem

To address the limitations, we quantize the significance and correlation of each HP to determine the feasibility of the search space $\mathcal{X}$ in Section 4.1. In Section 4.2, we visualize the HPs that determine the curvature of (2). To reduce the evaluation cost in (3), we analyze the approximation methods in Section 4.3. Following (Ruffinelli et al., 2019), the experiments runs on the seven embedding models in Section 2 and two widely used datasets WN18RR (Dettmers et al., 2017) and FB15k-237 (Toutanova and Chen, 2015). The experiments are are implemented with PyTorch framework (Paszke et al., 2017), on a machine with two Intel Xeon 6230R CPUs, 754 GB memory and eight RTX 3090 GPUs with 24 GB memories each. We provide the implementation details in the Appendix D.1 and code at `https://anonymous.4open.science/r/TOSS-ACL2022/`.

4.1 Search space: $\mathbf{x} \in \mathcal{X}$

Considering the large amount of HP configurations in $\mathcal{X}$, we take the simple and efficient approach where HPs are evaluated under control variate (Hutter et al., 2014; You et al., 2020), which varies the i-th HP while fixing the other HPs. First, we discretize the continuous HPs according to their ranges. Then the feasibility of the search space $\mathcal{X}$ is analyzed by checking the ranking distribu-

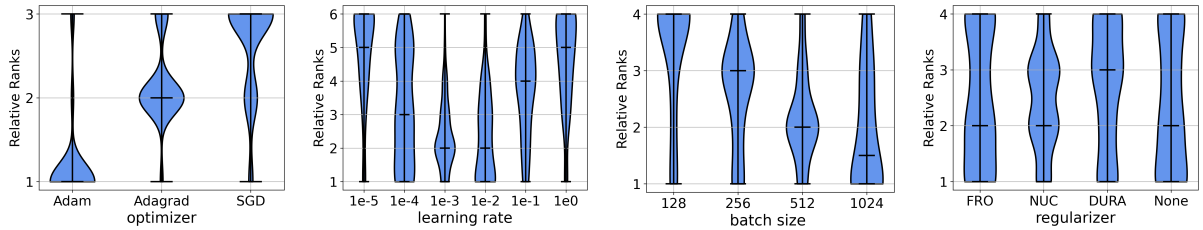

Figure 2: Ranking distribution of selected HPs. A value with larger area in the bottom indicates the higher ranking of this value. The four figures correspond to the four groups: fixed choice, limited range, monotonously related, no obvious patterns. Full results are in the Appendix B.2.

tion and consistency of individual HPs. These can help us reduce and decouple the search space. The detailed setting for this part is in the Appendix B.1.

Ranking distribution. To reduce the search space, we use the ranking distribution to indicate what HP values perform consistently. Given an anchor configuration $\mathbf{x}$, we obtain the ranking of different values $\theta \in X_i$, where X_i the range of the i-th HP, by fixing the other HPs. The ranking distribution is then collected over different anchor configurations in $\mathcal{X}_i$, different models and datasets. According to the violin plots of ranking distribution shown in Figure 2, the HPs can be classified into four groups:

(a). *fixed choice*, e.g., Adam is the best optimizer and inverse relation should not be introduced;
(b). *limited range*, e.g., learning rate, reg. weight and dropout rate are better in certain ranges;
(c). *monotonously related*: e.g., larger batch size and dimension size tend to be better;
(d). *no obvious patterns*: e.g., the remaining HPs.

Consistency. To decouple the search space, we measure the consistency of configurations' rankings while varying only one HP. If the ranking of configurations' performance is consistent with different values of $\theta \in X_i$, we can decouple the search procedure of the i-th HP with the others. We use spearman's ranking correlation coefficient (SRCC) (Schober et al., 2018) to indicate such consistency. Given a set $\mathcal{X}_i$ of anchor configurations with two different values $\theta_1, \theta_2 \in X_i$, SRCC measures the strength of the association between configurations' rankings in $\mathcal{X}_i$ with $x_i = \theta_1$ and with $x_i = \theta_2$. The consistency of the i-th HP is measured by averaging the SRCC over the different pairs of $\theta_1, \theta_2 \in X_i$, the different models and datasets. The larger consistency (in the range $[-1, 1]$) indicates that changing the value of the i-th HP does not influence much on the configurations' ranking. Please refer to Appendix B.2 for detailed forms for consistency.

As in Figure 3, the batch size and dimension size show higher consistency than the other HPs. Hence, the evaluation of the configurations can be

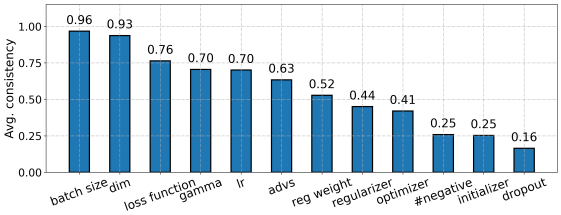

Figure 3: Consistency of each HP.

consistent with different choices of them. This indicates that we can decouple the search of batch size and dimension size with the other HPs.

4.2 Validation curvature: $\mathcal{M}(\cdot, \cdot)$

We analyze the curvature of the validation performance $\mathcal{M}(\cdot, \cdot)$ w.r.t $\mathbf{x} \in \mathcal{X}$. Specifically, we follow (Li et al., 2017) to visualize the validation loss landscape by uniformly varying the numerical HPs in two directions (20 configurations in each direction) on the model ComplEx and dataset WN18RR. From Figure 4(a), we observe that the curvature is quite complex with many local maximum areas.

To learn experience from the evaluated configurations and guide the next configuration sampling, we learn a surrogate model as a predictor to approximate the validation curvature. The curvatures of three common surrogates, i.e., Gaussian process (GP) (Williams and Rasmussen, 1995), multi layer perceptron (MLP) (Gardner and Dorling, 1998), and random forest (RF) (Breiman, 2001), are in Figure 4(b)-4(d). The surrogate models are trained with 100 random configurations in the search space. As shown, both GP and MLP fail to capture the complex local surface in Figure 4(a) as they tend to learn a flat and smooth distribution in the search space. In comparison, RF is better in capturing the local distributions. Hence, we regard RF as a better choice in the search space. A more detailed comparison on the approximation ability of different surrogates is in the Appendix B.3.

4.3 Evaluation cost: $\arg\min_{\boldsymbol{P}} \mathcal{L}$

The evaluation cost is the majority computation cost in HP search. In this part, we firstly evalu-

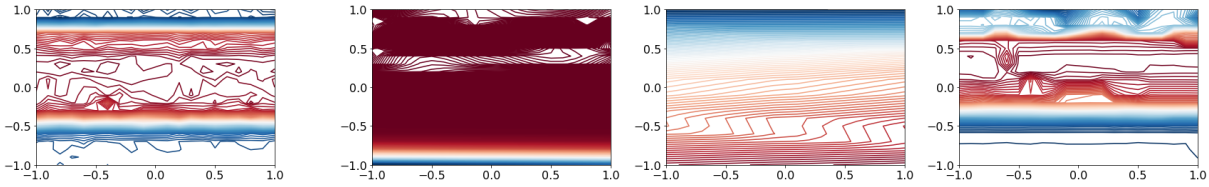

(a) Ground truth (b) GP prediction (c) MLP prediction (d) RF prediction

Figure 4: Curvature of the search space and three surrogate models.

ate the HPs that have influence on the evaluation cost. Then, we analyze the evaluation transferability from small subgraph to the whole graph.

Cost of different HPs. The cost of each HP value $\theta \in X_i$ is averaged over the different anchor configurations in $\mathcal{X}_i$, different models and datasets. We find that the evaluation cost increase significantly with larger batch size and dimension size, while the number of negative samples and choice of loss function and regularizer do not have much influence on the cost. We provide two exemplar curves in Figure 5 and put the remaining results in the Appendix B.4.

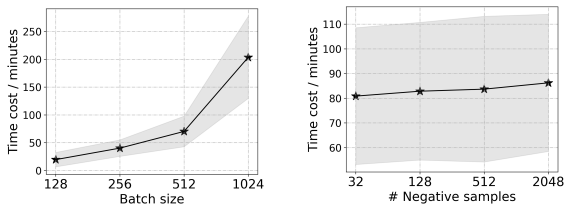

Figure 5: Computing time cost. The dots are the average and the shades are the standard deviation.

Transferability of subgraphs. Subgraphs can efficiently approximate the properties in the whole graph (Hamilton et al., 2017; Teru et al., 2020). We understand the impact of subgraph sampling on HP search by checking the evaluation consistency between small subgraphs and the whole graph.

First, we study how to sample subgraphs. There are several approaches to sample small subgraphs from a large graph (Leskovec and Faloutsos, 2006). We compare four representative approaches in Figure 6, i.e., Pagerank node sampling (Pagerank), random edge sampling (Random edge), single-start random walk (single-RW) and multi-start random walk (multi-RW). For a fair comparison, we constrain the subgraphs with about 20% entities. The consistency between the sampled subgraph with the whole graph is evaluated by the SRCC in (4). We observe that multi-start random walk is the best among the different sampling methods.

Apart from directly transferring the evaluation from subgraph to whole graph, we can alternatively train a predictor with observations on subgraphs

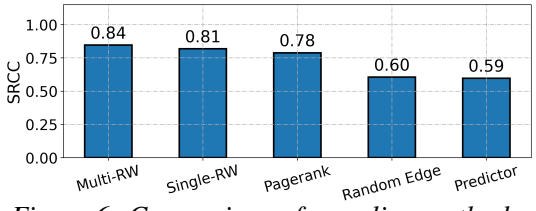

Figure 6: Comparison of sampling methods.

and then transfers the model to predict the configuration performance on the whole graph. From Figure 6, we find that directly transferring evaluations from subgraphs to the whole graph is much better than transferring the predictor model.

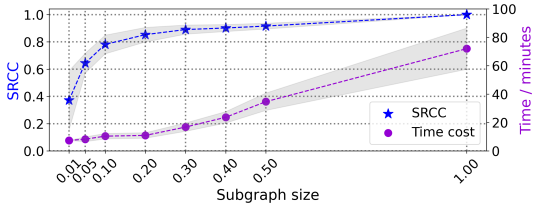

Figure 7: Consistency and cost of different subgraph sizes. The shades are the standard deviation.

In addition, we show the consistency and cost in terms of different subgraph sizes (percentage of entities to the whole graph) in Figure 7. As shown, evaluation on subgraphs can significantly improve efficiency. When the scale increases, the consistency increases but the cost increases. To balance the consistency and cost, the subgraphs with 20% entities are the better choices.

5 Efficient search algorithm

By analyzing the ranking distribution and consistency of HPs in Section 4.1, we observe that not all the HP values are equivalently good, and some HPs can be decoupled, this motivates us to revise the search space in Section 5.1. Based on the analysis in Section 4.2 and Section 4.3, we then propose an efficient two-stage algorithm in Section 5.2

5.1 Reduce and decouple the search space

To reduce the search space, we mainly consider groups (a) and (b) of HPs in Section 4.1. From the full results in the Appendix B.2, we observe that Adam can consistently perform better than the other two optimizers, the learning rate can be

better in the range $[10^{-4}, 10^{-1}]$, the regularization weight is better in $[10^{-8}, 10^{-2}]$, dropout rate is better in $[0, 0.3]$, and add inverse relation is not a good choice.

To decouple the search space, we consider batch size and dimension that have larger consistency values than the others and are monotonously related to the performance as in group (c). However, the computation costs of batch size and dimension size increase prominently as in Figure 5. Hence, we can set batch size as 128 and dimension size as 100 to search the other HPs with low evaluation cost and increase their values in a fine-tuning stage.

Given the full search space $\mathcal{X}$, we denote the reduced space as $\tilde{\mathcal{X}}$ and the further decoupled space as $\hat{\mathcal{X}}$. The changes from $\mathcal{X}$ to $\hat{\mathcal{X}}$ are in the Appendix C, with hundreds times reduction in size.

5.2 Two-stage search algorithm (TOSS)

As discussed in Section 4.3, the evaluation cost can be significantly reduced with small batch size, dimension size and subgraph. This motivates us to design a two-stage search algorithm, named TOSS, as in Figure 1(b) and Algorithm 1.

- In the first stage, we sample a subgraph G with 20% entities from the whole graph D_{tra} by multi-start random walk. Based on the curvature understanding in Section 4.2, we use the surrogate model random forest (RF) under the state-of-the art framework BORE (Tiao et al., 2021), denoted as RF+BORE, to explore HPs in $\hat{\mathcal{X}}$ on the subgraph G in steps 3-7. The top 10 configurations evaluated in this stage are saved in a set $\hat{\mathcal{X}}^*$.
- In the second stage, we increase batch size and dimension size for configurations in $\hat{\mathcal{X}}^*$ to generate a new set $\tilde{\mathcal{X}}^*$. Then, the configurations in $\tilde{\mathcal{X}}^*$ are searched by the RF+BORE again in steps 11-16 until the remaining $B/2$ budget exhausted.

Finally, the configuration $\mathbf{x}^*$ achieving the best performance on D_{val} is returned for testing.

5.3 Discussion

In this part, we summarize the main difference of TOSS with the existing HP search algorithms, i.e. Random (random search) (Bergstra and Bengio, 2012), Hyperopt (Bergstra et al., 2013), SMAC (Hutter et al., 2011), RF+BORE (Tiao et al., 2021), and AutoNE (Tu et al., 2019). The comparison is on three aspects, i.e., search space, surrogate model and fast evaluation, in Table 2. TOSS reduces and decouples the search space based on the understanding of HPs' properties and uses the surrogate RF based on the understanding on validation curvature. The fast evaluation on subgraph in TOSS selects the top10 configurations to directly transfer for fine-tuning, while AutoNE (Tu et al., 2019) just uses fast evaluation on subgraphs to train the surrogate model and transfers the surrogate model for HP search on whole graph. However, the transferability of the surrogate model is shown to be much worse than direct transfer as in Figure 6.

Algorithm 1 TOSS: two-stage search algorithm

Require: KG embedding model F, dataset D, and budget B;
1: reduce the search space $\mathcal{X}$ to $\tilde{\mathcal{X}}$ and decouple $\tilde{\mathcal{X}}$ to $\hat{\mathcal{X}}$;
 # state one: *efficient evaluation on subgraph*
2: sample a subgraph (with 20% entities) G from D_{tra} by multi-start random walk;
3: **repeat**
4: sample a configuration $\hat{\mathbf{x}}$ from $\hat{\mathcal{X}}$ by RF+BORE;
5: evaluate $\hat{\mathbf{x}}$ on the subgraph G to get the performance;
6: update the RF with record $\big(\hat{\mathbf{x}}, \mathcal{M}(F(P^*, \hat{\mathbf{x}}), G_{\text{val}})\big)$;
7: **until** $B/2$ budget exhausted;
8: save the top10 configurations in $\hat{\mathcal{X}}^*$;
 # state two: *fine-tune the top configurations*
9: increase the batch/dimension size in $\hat{\mathcal{X}}^*$ to get $\tilde{\mathcal{X}}^*$;
10: set $y^* = 0$ and initialize the RF surrogate;
11: **repeat**
12: select a configuration $\tilde{\mathbf{x}}^*$ from $\tilde{\mathcal{X}}^*$ by RF+BORE;
13: evaluate on whole graph G to get the performance;
14: update the RF with record $\big(\tilde{\mathbf{x}}^*, \mathcal{M}(F(P^*, \tilde{\mathbf{x}}^*), D_{\text{val}})\big)$;
15: **if** $\mathcal{M}(F(P^*, \tilde{\mathbf{x}}^*), D_{\text{val}}) > y^*$ **then** $y^* \leftarrow \mathcal{M}(F(P^*, \tilde{\mathbf{x}}^*), D_{\text{val}})$ and $\mathbf{x}^* \leftarrow \tilde{\mathbf{x}}^*$; **end if**
16: **until** $B/2$ budget exhausted;
17: **return** $\mathbf{x}^*$.

Table 2: Comparison of HP search algorithms.

	search space		surrogate	fast
	reduce	decouple	model	evaluation
Random	×	×	×	×
Hyperopt	×	×	TPE	×
Ax	×	×	GP	×
SMAC	×	×	RF	×
RF+BORE	×	×	RF	×
AutoNE	×	×	GP	√
TOSS	√	√	RF	√

6 Empirical evaluation

6.1 Overall performance

In this part, we compare the proposed algorithm TOSS with six HP search algorithms in Table 2. For AutoNE, we allocate half budget for it to search on subgraph and another half budget to search on the whole graph with the transferred surrogate model. The baselines search in the full search space (in Table 1) with the same amount of budget (one day's clock time) as TOSS. We use mean reciprocal ranking (MRR, the larger the better) (Bordes et al., 2013) to indicate the performance.

In Figure 8 left, we show the best performance

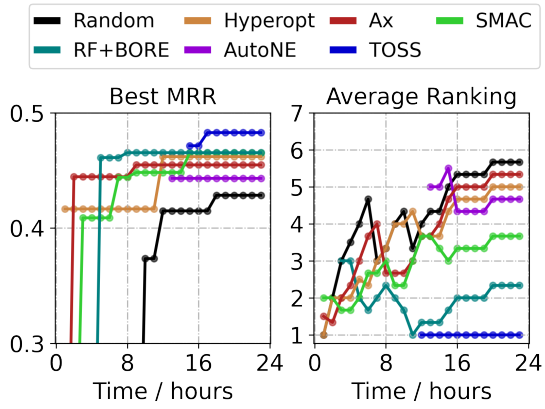

Figure 8: Search algorithm comparison (viewed in color). The dots are the results collected per hour.

achieved along the clock time in one experiment on model ComplEx and dataset WN18RR, and in Figure 8 right, the ranking of each algorithm averaged over all the models and datasets. Since AutoNE and TOSS run on the subgraphs in the first stage, the starting points of them locate after 12 hours. The starting point of TOSS is a bit later since it constrains to use large batch size and dimension size, which is more expensive, in the second stage. As shown, random search is the worst due to the full randomness. SMAC and RF+BORE achieve better performance than Hyperopt and Ax since RF can fit the space better than TPE and GP as in Section 4.2. Due to the weak transferability of predictor (see Figure 6) and weak approximation ability of GP (see Figure 4), AutoNE also performs bad. TOSS is much better than all the baselines. We show the full search process of the two-stage algorithms AutoNE and TOSS in Figure 9(a). By exploring sufficient configurations in the first stage, the configurations fine-tuned in the second stage can consistently achieve the best performance.

We show the reproduced results on seven embedding models, i.e., TransE, RotatE, RESCAL, DistMult, ComplEx, TuckER, and ConvE, on WN18RR and FB15k-237 with HPs searched by TOSS are in the Appendix D.2. Overall, TOSS achieves better performance compared with the original reported results and the reproduced results in (Ruffinelli et al., 2019). We observe that the tensor factorization models such as RESCAL, ComplEx and TuckER have better performance than the translational distance models TransE, RotatE and neural network model ConvE. This conforms with the theoretical analysis that tensor factorization models are more expressive (Wang et al., 2018).

To further demonstrate the advantage of TOSS, we apply it to the Open Graph Benchmark (OGB) (Hu et al., 2020). OGB is a collection of realistic and large-scale benchmark datasets for machine learning on graphs. Many embedding models have been tested there by two large-scale KG for link prediction, i.e., ogbl-biokg and ogbl-wikikg2. Due to their scale, the graph neural network based models cannot be applied.

We use TOSS to search HPs for embedding models, i.e., TransE, RotatE, ComplEx and DistMult, on OGB. Since the computation costs of the two datasets are much higher, we set the time budget as 5 days. All the compared embedding models in TOSS are constrained to have the same (or lower) number of model parameters[1] compared with the reported models in (Hu et al., 2020). More details on model parameters, standard derivation, and validation performance are in the Appendix D.3. As shown in Table 3, TOSS consistently improves the performance of the four embedding models with the same or fewer parameters compared with the results on the OGB board.

Table 3: Performance in MRR in OGB link prediction board `https://ogb.stanford.edu/docs/leader_linkprop/` *and those reproduced by TOSS on ogbl-biokg and ogbl-wikikg2. Relative improvements are in parenthesize.*

models		ogbl-biokg	ogbl-wikikg2
OGB board	TransE	0.7452	0.4256
	RotatE	0.7989	0.2530
	DistMult	0.8043	0.3729
	ComplEx	0.8095	0.4027
TOSS	TransE	0.7771 (4.28%↑)	0.4745 (11.48%↑)
	RotatE	0.8018 (0.36%↑)	0.2845 (12.45%↑)
	DistMult	0.8254 (2.62%↑)	0.4866 (30.49%↑)
	ComplEx	0.8383 (3.55%↑)	0.4898 (21.62%↑)
average improvement		2.70%	19.01%

6.2 Ablation study

In this section, we probe into how important and sensitive the various components of TOSS are.

Space comparison. To demonstrate the effectiveness gained by reducing and decoupling the search space, we compare the following variants: (i) RF+BORE on the full space $\mathcal{X}$; (ii) RF+BORE on the reduced space $\tilde{\mathcal{X}}$; (iii) RF+BORE on the decoupled space $\hat{\mathcal{X}}$, which differs from TOSS by searching on the whole graph in the first stage; and (iv) TOSS in Algorithm 1. All the variants have one day's budget. As in Figure 9(b), the size of

[1] We run all models on ogbl-wikikg2 with 100 dimension size to avoid out-of-memory, instead of 500 on OGB board.

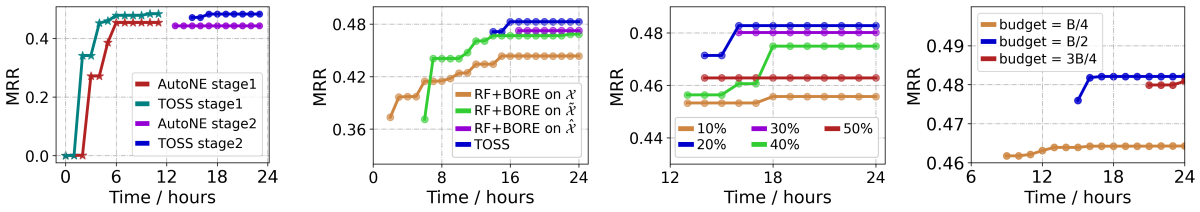

(a) Full search processes (b) Search space (c) Subgraph size (d) First-stage budget

Figure 9: (a): full search processes of the two-stage algorithms. (b-d): ablation studies on TOSS. Model ComplEx and dataset WN18RR are used in these experiments.

search space matters for the search efficiency. The three components, i.e., space reduction, space decoupling, and fast evaluation on subgraph, are all important to the success of TOSS.

Size of subgraphs. We show the influence of subgraph sizes with different ratios of entities (10%, 20%, 30%, 40%, 50%) in Figure 9(c). Using subgraphs with too large or too small size is not guaranteed to find good configurations. Based on the understanding in Figure 7, the subgraphs with small size have poor transferability and those with large size are expensive to evaluate. Hence, we should balance the transferability and evaluation cost by sampling subgraphs with $20\% \sim 30\%$ entities.

Budget allocation. In Algorithm 1, we allocate $B/2$ budget for both the first and second stage. Here, we show the performance of different allocation ratios, i.e., $B/4$, $B/2$, and $3B/4$ in the first stage and the remaining budget in the second stage. As in Figure 9(d), allocating too many or too few budgets to the first stage is not good. It either fails to explore sufficient configurations in the first stage or only fine-tunes a few configurations in the second stage. Allocating the same budget to the two stages is in a better trade-off.

7 Related works

Our work is not the first in analyzing the KG embedding models. Ruffinelli et al. (2019) pointed out that the earlier works in KG embedding only search HPs in small grids. By searching hundreds of HPs in a unified framework, the reproduced performance can be significantly improved. Similarly, Ali et al. (2020) proposed another unified framework to evaluate different models. Rossi et al. (2021) evaluated 16 different models and analyzed their properties on different datasets. All of these works emphasize the importance of HP search, but none of them provide efficient algorithms to search HPs for KG embedding models.

Understanding the HPs in a large search space is non-trivial since many HPs only have moderate impact on the model performance (Ruffinelli et al., 2019) and jointly evaluate them requires a large number of experiments (Fawcett and Hoos, 2016; Probst et al., 2019). Considering the huge amount of HP configurations (with 10^5 categorical choices and 5 continuous values), it is extremely expensive to exhaustively evaluate most of them. Hence, we adopt control variate experiments to efficiently evaluate HPs' properties instead of the quasi-random search in (Ruffinelli et al., 2019; Ali et al., 2020).

Technically, AutoNE (Tu et al., 2019) and e-AutoGR (Wang et al., 2021) are similar to ours by leveraging subgraphs to improve search efficiency on graph learning. Since they do not target at KG embedding methods, directly adopt them here is not a good choice. Based on the understanding in this paper, we demonstrate that transferring the surrogate model from subgraph evaluation to the whole graph is inferior to directly transferring the top configurations for KG embedding models.

8 Conclusion

In this paper, we analyze the HPs' properties in KG embedding models with search space size, validation curvature and evaluation cost. We observe that some HP values in the search space are not equivalently good, the batch size and dimension size can be decoupled with the other HPs, the curvature can be better approximated by random forest, and that subgraphs can help improve evaluation efficiency with high consistency. Based on the observations, we propose an efficient search algorithm TOSS that efficiently explores configurations in a decoupled space on small subgraphs and then fine-tunes the top configurations. Empirical evaluations show that TOSS is robuster and more efficient than the conventional HP search algorithms and achieves competing performance on large-scale KGs in open graph benchmarks. In the future work, we will understand the graph neural network based models and apply TOSS on them to solve the scaling limitations in HP search.

References

Mehdi Ali, Max Berrendorf, Charles Tapley Hoyt, Laurent Vermue, Mikhail Galkin, Sahand Sharifzadeh, Asja Fischer, Volker Tresp, and Jens Lehmann. 2020. Bringing light into the dark: A large-scale evaluation of knowledge graph embedding models under a unified framework. Technical report, arXiv:2006.13365.

Ivana Balažević, Carl Allen, and Timothy M Hospedales. 2019. Tucker: Tensor factorization for knowledge graph completion. In *EMNLP*.

James Bergstra, Rémi Bardenet, Yoshua Bengio, and Balázs Kégl. 2011. Algorithms for hyper-parameter optimization. In *NIPS*, pages 2546–2554.

James Bergstra and Yoshua Bengio. 2012. Random search for hyper-parameter optimization. *JMLR*, 13(2).

James Bergstra, Dan Yamins, David D Cox, et al. 2013. Hyperopt: A python library for optimizing the hyperparameters of machine learning algorithms. In *Proceedings of the 12th Python in science conference*, volume 13, page 20. Citeseer.

Antoine Bordes, Sumit Chopra, and Jason Weston. 2014. Question answering with subgraph embeddings. In *EMNLP*.

Antoine Bordes, Nicolas Usunier, Alberto Garcia-Duran, Jason Weston, and Oksana Yakhnenko. 2013. Translating embeddings for modeling multi-relational data. In *NeurIPS*, pages 2787–2795.

Leo Breiman. 2001. Random forests. *ML*, 45(1):5–32.

Liwei Cai and William Yang Wang. 2018. Kbgan: Adversarial learning for knowledge graph embeddings. In *NAACL*, pages 1470–1480.

Marc Claesen and Bart De Moor. 2015. Hyperparameter search in machine learning. Technical report, arXiv:1502.02127.

Benoît Colson, Patrice Marcotte, and Gilles Savard. 2007. An overview of bilevel optimization. *Ann. Oper. Res.*, 153(1):235–256.

Tim Dettmers, Pasquale Minervini, Pontus Stenetorp, and Sebastian Riedel. 2017. Convolutional 2D knowledge graph embeddings. In *AAAI*.

John Duchi, Elad Hazan, and Yoram Singer. 2011. Adaptive subgradient methods for online learning and stochastic optimization. *JMLR*, 12(7).

Chris Fawcett and Holger H Hoos. 2016. Analysing differences between algorithm configurations through ablation. *Journal of Heuristics*, 22(4):431–458.

Matt W Gardner and SR Dorling. 1998. Artificial neural networks (the multilayer perceptron) – a review of applications in the atmospheric sciences. *Atmospheric environment*, 32(14-15):2627–2636.

Ian Goodfellow, Yoshua Bengio, and Aaron Courville. 2016. *Deep learning*. MIT press.

Lingbing Guo, Zequn Sun, and Wei Hu. 2019. Learning to exploit long-term relational dependencies in knowledge graphs. In *ICML*, pages 2505–2514.

William L Hamilton, Rex Ying, and Jure Leskovec. 2017. Inductive representation learning on large graphs. In *NIPS*, pages 1025–1035.

Weihua Hu, Matthias Fey, Marinka Zitnik, Yuxiao Dong, Hongyu Ren, Bowen Liu, Michele Catasta, and Jure Leskovec. 2020. Open graph benchmark: Datasets for machine learning on graphs. *NeurIPS*.

Frank Hutter, Holger Hoos, and Kevin Leyton-Brown. 2014. An efficient approach for assessing hyperparameter importance. In *ICML*, pages 754–762. PMLR.

Frank Hutter, Holger H Hoos, and Kevin Leyton-Brown. 2011. Sequential model-based optimization for general algorithm configuration. In *ICLIO*, pages 507–523. Springer.

Shaoxiong Ji, Shirui Pan, Erik Cambria, Pekka Marttinen, and S Yu Philip. 2021. A survey on knowledge graphs: Representation, acquisition and applications. *TNNLS*.

Seyed Mehran Kazemi and David Poole. 2018. SimplE embedding for link prediction in knowledge graphs. In *NeurIPS*.

Diederik P Kingma and Jimmy Ba. 2014. Adam: A method for stochastic optimization. In *ICLR*.

Timothée Lacroix, Nicolas Usunier, and Guillaume Obozinski. 2018. Canonical tensor decomposition for knowledge base completion. In *ICML*, pages 2863–2872. PMLR.

Jure Leskovec and Christos Faloutsos. 2006. Sampling from large graphs. In *SIGKDD*, pages 631–636.

Hao Li, Zheng Xu, Gavin Taylor, Christoph Studer, and Tom Goldstein. 2017. Visualizing the loss landscape of neural nets. In *NIPS*.

Maximilian Nickel, Volker Tresp, and Hans-Peter Kriegel. 2011. A three-way model for collective learning on multi-relational data. In *ICML*, volume 11, pages 809–816.

Adam Paszke, Sam Gross, Soumith Chintala, Gregory Chanan, Edward Yang, Zachary DeVito, Zeming Lin, Alban Desmaison, Luca Antiga, and Adam Lerer. 2017. Automatic differentiation in pytorch.

Philipp Probst, Anne-Laure Boulesteix, and Bernd Bischl. 2019. Tunability: importance of hyperparameters of machine learning algorithms. *JMLR*, 20(1):1934–1965.

Carl Edward Rasmussen. 2003. Gaussian processes in machine learning. In *Summer school on machine learning*, pages 63–71. Springer.

Andrea Rossi, Denilson Barbosa, Donatella Firmani, Antonio Matinata, and Paolo Merialdo. 2021. Knowledge graph embedding for link prediction: A comparative analysis. *TKDD*.

Daniel Ruffinelli, Samuel Broscheit, and Rainer Gemulla. 2019. You can teach an old dog new tricks! on training knowledge graph embeddings. In *ICLR*.

Apoorv Saxena, Aditay Tripathi, and Partha Talukdar. 2020. Improving multi-hop question answering over knowledge graphs using knowledge base embeddings. In *ACL*, pages 4498–4507.

Michael Schlichtkrull, Thomas N Kipf, Peter Bloem, Rianne Van Den Berg, Ivan Titov, and Max Welling. 2018. Modeling relational data with graph convolutional networks. In *ESWC*, pages 593–607. Springer.

Patrick Schober, Christa Boer, and Lothar A Schwarte. 2018. Correlation coefficients: appropriate use and interpretation. *Anesthesia & Analgesia*, 126(5):1763–1768.

Jasper Snoek, Hugo Larochelle, and Ryan P Adams. 2012. Practical bayesian optimization of machine learning algorithms. *NIPS*, 25.

Zhiqing Sun, Zhi-Hong Deng, Jian-Yun Nie, and Jian Tang. 2019. Rotate: Knowledge graph embedding by relational rotation in complex space. In *ICLR*.

Zhiqing Sun, Shikhar Vashishth, Soumya Sanyal, Partha Talukdar, and Yiming Yang. 2020. A re-evaluation of knowledge graph completion methods. In *ACL*, pages 5516–5522.

Komal Teru, Etienne Denis, and Will Hamilton. 2020. Inductive relation prediction by subgraph reasoning. In *ICML*, pages 9448–9457. PMLR.

Louis C Tiao, Aaron Klein, Matthias Seeger, Edwin V Bonilla, Cedric Archambeau, and Fabio Ramos. 2021. Bore: Bayesian optimization by density-ratio estimation. In *ICML*.

Kristina Toutanova and Danqi Chen. 2015. Observed versus latent features for knowledge base and text inference. In *ACL Workshop*, pages 57–66.

Théo Trouillon, Christopher R Dance, Johannes Welbl, Sebastian Riedel, Éric Gaussier, and Guillaume Bouchard. 2017. Knowledge graph completion via complex tensor factorization. *JMLR*, 18(1):4735–4772.

Ke Tu, Jianxin Ma, Peng Cui, Jian Pei, and Wenwu Zhu. 2019. Autone: Hyperparameter optimization for massive network embedding. In *SIGKDD*, pages 216–225.

Shikhar Vashishth, Soumya Sanyal, Vikram Nitin, and Partha Talukdar. 2020. Composition-based multi-relational graph convolutional networks. *ICLR*.

Quan Wang, Zhendong Mao, Bin Wang, and Li Guo. 2017. Knowledge graph embedding: A survey of approaches and applications. *TKDE*, 29(12):2724–2743.

Xin Wang, Shuyi Fan, Kun Kuang, and Wenwu Zhu. 2021. Explainable automated graph representation learning with hyperparameter importance. In *ICML*, pages 10727–10737. PMLR.

Yanjie Wang, Rainer Gemulla, and Hui Li. 2018. On multi-relational link prediction with bilinear models. In *AAAI*.

Christopher KI Williams and Carl Edward Rasmussen. 1995. Gaussian processes for regression. In *NIPS*, pages 514–520.

Bishan Yang, Wen-tau Yih, Xiaodong He, Jianfeng Gao, and Li Deng. 2015. Embedding entities and relations for learning and inference in knowledge bases. In *ICLR*.

Jiaxuan You, Zhitao Ying, and Jure Leskovec. 2020. Design space for graph neural networks. *NeurIPS*, 33.

Fuzheng Zhang, Nicholas Jing Yuan, Defu Lian, Xing Xie, and Wei-Ying Ma. 2016. Collaborative knowledge base embedding for recommender systems. In *SIGKDD*, pages 353–362.

Yongqi Zhang, Quanming Yao, and Lei Chen. 2021. Simple and automated negative sampling for knowledge graph embedding. *VLDB-J*, 30(2):259–285.

Zhanqiu Zhang, Jianyu Cai, and Jie Wang. 2020. Duality-induced regularizer for tensor factorization based knowledge graph completion. *NeurIPS*, 33.

A Details of the search space

Denote a knowledge graph as $\mathcal{G} = \{E, R, D\}$, where E is the set of entities, R is the set of relations, and D is the set of triplets with training/validation/test splits $D = D_{\text{tra}} \cup D_{\text{val}} \cup D_{\text{tst}}$.

Basically, the KG embedding models use a scoring function f and the model parameters $\boldsymbol{P}$ to measure the plausibility of triplets. We learn the embeddings such that the positive and negative triplets can be separated by f and $\boldsymbol{P}$. In Table 4, we provide the forms f of the embedding model we used to evaluate the search space $\mathcal{X}$ in Section 3.

Table 4: Definitions of the embedding models. $\circ$ is a rotation operation in the complex value space; $\otimes$ is the Hermitian dot product in the complex value space; $Re(\cdot)$ returns the real part of a complex value; $\mathcal{W}_{i,j,k}$ is the ijk-th element in a core tensor $\mathcal{W} \in \mathbb{R}^{d \times d \times d}$; and conv is a convolution operator on the head and relation embeddings. For more details, please refer to the corresponding references.

model type	model	$f(h, r, t)$	embeddings
translational distance	TransE (Bordes et al., 2013)	$-\lVert \boldsymbol{h} + \boldsymbol{r} - \boldsymbol{t} \rVert_1$	$\boldsymbol{h}, \boldsymbol{r}, \boldsymbol{t} \in \mathbb{R}^d$
	RotatE (Sun et al., 2019)	$-\lVert \boldsymbol{h} \circ \boldsymbol{r} - \boldsymbol{t} \rVert_{c1}$	$\boldsymbol{h}, \boldsymbol{r}, \boldsymbol{t} \in \mathbb{C}^d$
tensor factorization	RESCAL (Nickel et al., 2011)	$\boldsymbol{h}^\top \cdot \boldsymbol{R}_r \cdot \boldsymbol{t}$	$\boldsymbol{h}, \boldsymbol{t} \in \mathbb{R}^d, \boldsymbol{R}_r \in \mathbb{R}^{d \times d}$
	DistMult (Yang et al., 2015)	$\boldsymbol{h}^\top \cdot \text{diag}(\boldsymbol{r}) \cdot \boldsymbol{t}$	$\boldsymbol{h}, \boldsymbol{t}, \boldsymbol{r} \in \mathbb{R}^d$
	ComplEx (Trouillon et al., 2017)	$\boldsymbol{h}^\top \otimes \text{diag}(\boldsymbol{r}) \otimes \boldsymbol{t}$	$\boldsymbol{h}, \boldsymbol{t}, \boldsymbol{r} \in \mathbb{C}^d$
	TuckER (Balažević et al., 2019)	$\sum_i^d \sum_j^d \sum_k^d \mathcal{W}_{i,j,k} h_i \cdot r_j \cdot t_k$	$\boldsymbol{h}, \boldsymbol{t}, \boldsymbol{r} \in \mathbb{R}^d$
neural network	ConvE (Dettmers et al., 2017)	$\text{ReLU}(\text{conv}(\boldsymbol{h}, \boldsymbol{r}))^\top \cdot \boldsymbol{t}$	$\boldsymbol{h}, \boldsymbol{t}, \boldsymbol{r} \in \mathbb{R}^d$

A.1 Negative sampling

Since KG only contains positive triplets in D_{tra} (Wang et al., 2017), we should rely on the negative sampling to avoid trivial solutions of the embeddings. Given a positive triplet $(h, r, t) \in D_{\text{tra}}$, the corresponding set of negative triplets is represented as

$$D^-_{(h,r,t)} = \left\{(\tilde{h}, r, t) \notin D_{\text{tra}} : (h, r, t) \in D_{\text{tra}}, \tilde{h} \in E\right\} \cup \left\{(h, r, \tilde{t}) \notin D_{\text{tra}} : (h, r, t) \in D_{\text{tra}}, \tilde{t} \in E\right\}.$$

A common practice is to sample m negative triplets from $D^-_{(h,r,t)}$. The value of m can be any integer smaller than the number of entities. We follow (Sun et al., 2019) to sample from the range of m in $\{32, 128, 512, 2048\}$ for simplicity.

An alternative choice is to use all the negative triplets in $D^-_{(h,r,t)}$, leading to the 1VsAll (Lacroix et al., 2018) and kVsAll (Dettmers et al., 2017) settings.

- In 1VsAll, (h, r, t) is in the positive part and all the triplets in the set $\{(\tilde{h}, r, t) \notin D_{\text{tra}} : (h, r, t) \in D_{\text{tra}}, \tilde{h} \in E\}$ or $\{(h, r, \tilde{t}) \notin D_{\text{tra}} : (h, r, t) \in D_{\text{tra}}, \tilde{t} \in E\}$ are in the negative part;
- In kVsAll, the positive part contains all the triplets sharing the same head-relation pair or tail-relation part, i.e. $\{(h, r, t') \in D_{\text{tra}}\}$ or $\{(h', r, t) \in D_{\text{tra}}\}$, with the corresponding negative part $\{(h, r, \tilde{t}) \notin D_{\text{tra}} : (h, r, t) \in D_{\text{tra}}, \tilde{t} \in E\}$ or $\{(\tilde{h}, r, t) \notin D_{\text{tra}} : (h, r, t) \in D_{\text{tra}}, \tilde{h} \in E\}$.

Hence, the choice of negative sampling can be set in the range $\{32, 128, 512, 2048, \text{1VsAll}, \text{kVsAll}\}$.

A.2 Loss function

For simplicity, we denote D^+ and D^- as the sets of positive and negative triplets, respectively. Then, we summarize the commonly used loss functions as follows:

- Margin ranking (MR) loss. This loss ranks the positive triplets to have larger score than the negative triplets. Hence, the ranking loss is defined as

$$\mathcal{L} = \sum\nolimits_{(h,r,t) \in D^+} \sum\nolimits_{(\tilde{h},r,\tilde{t}) \in D^-} -\left|\gamma - f(h, r, t) + f(\tilde{h}, r, \tilde{t})\right|_+,$$

where $\gamma > 0$ is the margin value and $|a|_+ = \max(a, 0)$. The MR loss is widely used in early developed models, like TransE (Bordes et al., 2013) and DistMult (Yang et al., 2015). The value of γ, conditioned on MR loss, is another HP to search.

- Binary cross entropy (BCE) loss. It is typical to set the positive and negative triplets as a binary classification problem. Let the labels for the positive and negative triplets as $+1$ and -1 respectively, the BCE loss is defined as

$$\mathcal{L} = \sum\nolimits_{(h,r,t)\in D^+} \log\left(\sigma(f(h,r,t))\right) + \sum\nolimits_{(\tilde{h},r,\tilde{t})\in D^-} w_{(\tilde{h},r,\tilde{t})} \log\left(1-\sigma(f(\tilde{h},r,\tilde{t}))\right),$$

  where $\sigma(x) = \frac{1}{1+\exp(-x)}$ is the sigmoid function. The choice of $w_{(\tilde{h},r,\tilde{t})}$ leads to three different loss functions

  - BCE_mean (Sun et al., 2019), with $w_{(\tilde{h},r,\tilde{t})} = 1/|D^-_{(h,r,t)}|$.
  - BCE_sum (Dettmers et al., 2017), with $w_{(\tilde{h},r,\tilde{t})} = 1$.
  - BCE_adv (Sun et al., 2019), with

$$w_{(\tilde{h},r,\tilde{t})} = \frac{\exp(\alpha \cdot f(\tilde{h},r,\tilde{t}))}{\sum_{(h',r,t')\in D^-}\exp(\alpha \cdot f(h',r,t'))},$$

    where $\alpha > 0$ is the adversarial weight conditioned on BCE_adv loss.

- Cross entropy (CE) loss. Since the number of negative triplets is fixed, we can also regard the (h, r, t) as the true label over the negative ones. The loss can be written as

$$\mathcal{L} = \sum\nolimits_{(h,r,t)\in D^+} -f(h,r,t) + \log\left(\sum\nolimits_{(h',r,t')\in\{(h,r,t)\cup D^-\}} \exp(f(h',r,t'))\right),$$

  where the left part is the score of positive triplet and the right is the log sum scores of the joint set of positive and negative triplets.

A.3 Regularization

To avoid the embeddings increasing to unlimited values and reduce the model complexity, regularization techniques are often used. Denote $\boldsymbol{P}'$ as the embeddings participated in one iteration,

- the Frobenius norm is defined as the sum of L2 norms $r_{\text{FRO}} = \|\boldsymbol{P}'\|_2^2 = \sum_{ij} P'^2_{ij}$ (Yang et al., 2015);
- the NUC norm is defined as sum of L3 norms $r_{\text{FRO}} = \|\boldsymbol{P}'\|_3^3 = \sum_{ij} |P_{ij}|^3$ (Lacroix et al., 2018);
- DURA operates on triplets (Zhang et al., 2020). Denote $\boldsymbol{h}, \boldsymbol{r}, \boldsymbol{t}$ as the embeddings for the triplet (h, r, t), DURA constrains the composition of $\boldsymbol{h}$ and $\boldsymbol{r}$ to approximate $\boldsymbol{t}$ with $r_{\text{DURA}} = \|c(\boldsymbol{h}, \boldsymbol{r}) - \boldsymbol{t}\|_2^2$, where the composition function $c(\boldsymbol{h}, \boldsymbol{r})$ depends on corresponding scoring functions.

The regularization functions are then weighted by the regularization weight in the range $[10^{-12}, 10^2]$.

Apart from using explicit forms of regularization, we can also add dropout on the embeddings (Dettmers et al., 2017). Specifically, each dimension in the embeddings $\boldsymbol{h}, \boldsymbol{r}, \boldsymbol{t}$ will have a probability to be deactivated as 0 in each iteration. The probability is controlled by the dropout rate in the range $[0, 0.5]$. In some cases, working without regularization can also achieve good performance (Ali et al., 2020).

A.4 Optimization

To solve the learning problem, we should setup an appropriate optimization procedure. First, we can directly use the training set or add inverse relations to augment the data (Kazemi and Poole, 2018; Lacroix et al., 2018). This will not influence the training data, but will introduce additional parameters for the inverse relations. Second, we should choose the dimension of embeddings in small sizes $[100, 200]$ or large sizes $[500, 1000, 2000]$. Then, the embeddings are initialized by the initialization methods such as uniform, normal, xavier_norm, and xavier_uniform (Goodfellow et al., 2016). The optimization is conducted with optimizers like standard SGD, Adam (Kingma and Ba, 2014) and Adagrad (Duchi et al., 2011) with learning rate in the range $[10^{-5}, 0]$ Since the training is conducted on mini-batch, a batch size is determined in the range $\{128, 256, 512, 1024\}$.

B Details of HP understanding

In this part, we provide the details of configuration generation and the full results related to the HP understanding.

B.1 Configure generation

Since there are infinite numbers of values for a continuous HP, it is intractable to fully evaluate their ranges. To better analyze the continuous HPs, we discretize them in Table 5 according to their ranges. Then, for each HP $i = 1 \dots n$ with range X_i, we sample a set $\mathcal{X}_i \subset \mathcal{X}$ of s anchor configurations through quasi random search (Bergstra and Bengio, 2012) and uniformly dispute them to evaluate the different embedding models and datasets.

Table 5: Discretized HP values.

name	original range	discretized range
gamma	[1, 24]	$\{1, 6, 12, 24\}$
adv. weight	[0.5, 2.0]	{0.5, 1, 2}
reg. weight	$[10^{-12}, 10^{2}]$	10^2 in log scale
dropout rate	$[0, 0.5]$	0.1 in linear scale
learning rate	$[10^{-5}, 10^{0}]$	10^1 in log scale

We use the control variate experiments to evaluate each HP. For the i-th HP, we enumerate the values $\theta \in X_i$ for each anchor configuration $\mathbf{x} \in \mathcal{X}_i$, while fix the other HPs. In this way, we can observe the influence of x_i without the influence of the other HPs. For example, when evaluating the optimizers, we enumerate the optimizers Adam, Adagrad and SGD for the anchor configurations in $\mathcal{X}_i$. This generates a set of $|\mathcal{X}_i| \cdot |X_i|$ configurations. In this paper, the number of anchor configurations $|\mathcal{X}_i|$ is 175 for each HP.

B.2 Details for search space understanding

In this part, we add the ranking distribution of all the HPs. In addition, we also show the normalized MRR of each HP as a complementary. The normalization is conducted on each dataset with $\frac{y - y_{\min}}{y_{\max} - y_{\min}}$ such that the results of the HPs can be evaluated in the same value range.

The full results for the four types of HPs in Section 4.1 are provided in Figures 10-13. The larger area in the bottom in the voilin plots and the top area in the box plots indicate better performance. The HPs can be classified into four types:

(a). *fixed choices*: Adam is the fixed optimizer, and inverse relation is not preferred. See Figure 10.

(b). *limited range*: Learning rate, regularization weight and dropout rate should be limited in the ranges $[10^{-4}, 10^{-1}]$, $[10^{-12}, 10^{-2}]$ and $[0, 0.3]$, respectively. See Figure 11

(c). *monotonously related*: Batch size and dimension size have monotonic performance. The larger value tends to lead better results. See Figure 12.

(d). *no obvious patterns*: The choice of loss function, value of gamma, adversarial weight, number of negative samples, regularizer, initializer do not have obvious patterns. See Figure 13.

In addition, we provide the details of Spearman's ranking correlation coefficient (SRCC). Given a set of anchor configurations $\mathcal{X}_i$ to analyze the i-th HP, we denote $r(\mathbf{x}, \theta)$ as the rank of different $\mathbf{x} \in \mathcal{X}_i$ with fixed $x_i = \theta$. Then, the SRCC between two HP values $\theta_1, \theta_2 \in X_i$ is

$$\text{SRCC}(\theta_1, \theta_2) = 1 - \frac{\sum_{\mathbf{x} \in \mathcal{X}_i} |r(\mathbf{x}, \theta_1) - r(\mathbf{x}, \theta_2)|}{|\mathcal{X}_i| \cdot (|\mathcal{X}_i|^2 - 1)}, \tag{4}$$

where $|\mathcal{X}_i|$ means the number of anchor configurations in $\mathcal{X}_i$. We evaluate the consistency of the i-th HP by averaging the SRCC over the different pairs of $(\theta_1, \theta_2) \in X_i \times X_i$, the different models and datasets.

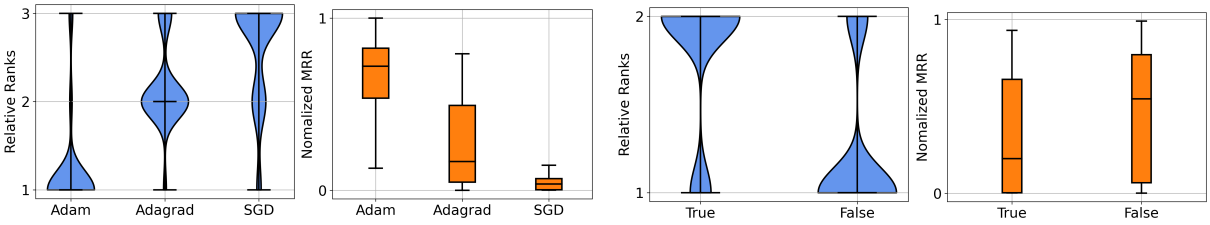

(a) optimizer (b) add inverse relation

Figure 10: HPs that have fixed choice since one configure has significant advantage.

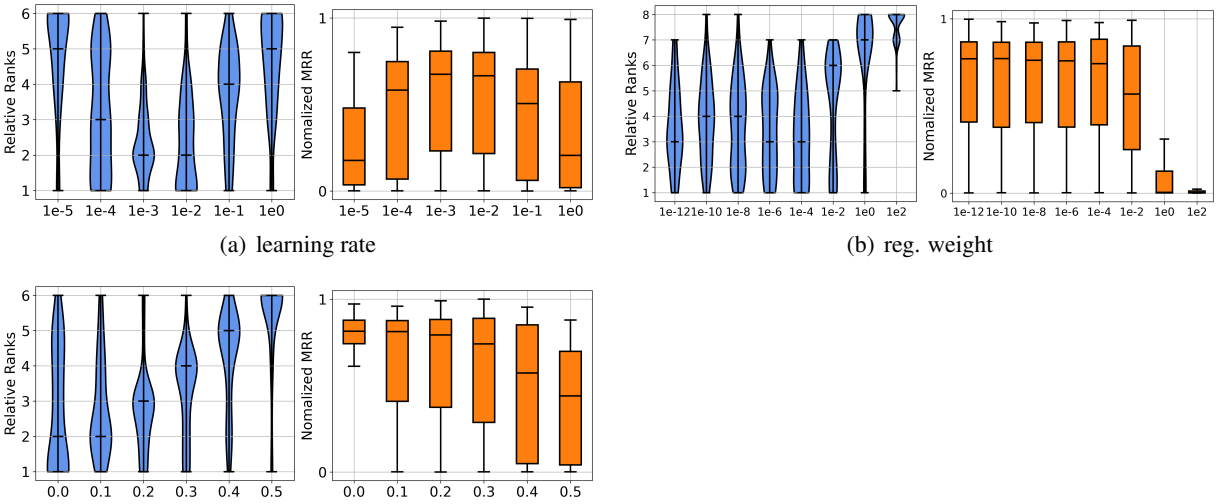

(a) learning rate (b) reg. weight

(c) dropout rate

Figure 11: HPs that have limited ranges since they only perform well in certain ranges.

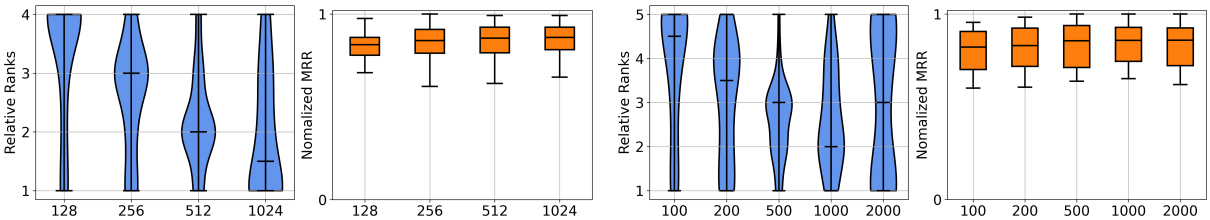

(a) batch_size (b) dimension

Figure 12: HPs that is monotonic with different choices of values.

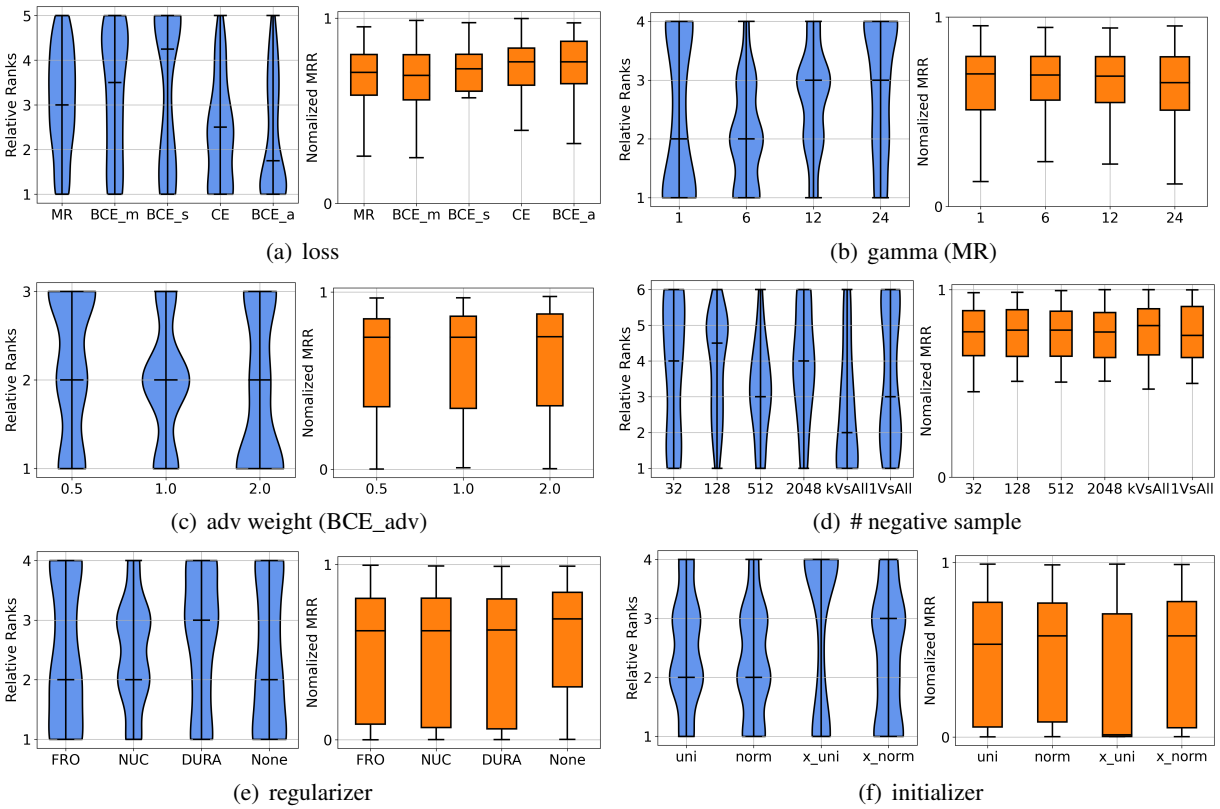

(a) loss (b) gamma (MR)

(c) adv weight (BCE_adv) (d) # negative sample

(e) regularizer (f) initializer

Figure 13: HPs that do not have obvious patterns. All of the values should be searched.

B.3 Approximation ability of surrogate models

In Section 4.2, we have shown that the curvature of a learned random forest (RF) model is more similar with the real curvature of the ground truth. Here, we further demonstrate this point through a synthetic experiment.

Specifically, 100 random configurations with evaluated performance are sampled. We use 10/20/30 random samples from them to train the surrogates since only a small number of HP configurations are available for the surrogate during searching. The remaining configurations are used for testing. Then, we evaluate the fitting ability of each model by the mean square error (MSE) of the estimated prediction to the target prediction. For GP (Rasmussen, 2003), we show the prediction with the Matern kernel used in AutoNE (Tu et al., 2019). For RF (Breiman, 2001), we build 200 tree estimators to fit the training samples. The MLP here (Gardner and Dorling, 1998) is designed as a three-layer feed-forward network with 100 hidden units and ReLU activation function in each layer. The average value and std of MSE over five different groups of configurations are shown in Table 6. As can been seen, random forest show much lower prediction error than GP and MLP with different number of training samples. This further demonstrates that RF can better fit such a complex HP search space.

Table 6: Comparison of different surrogate models in MSE.

# train configurations	10	20	30
GP	0.0693±0.02	0.029±0.01	0.019±0.01
MLP	2.121±0.4	2.052±0.3	0.584±0.1
RF	**0.003±0.002**	**0.002±0.001**	**0.001±0.001**

B.4 Results of cost evaluation

We show the average cost and standard derivation of five HPs, i.e. batch size, dimension size, number of negative samples, loss functions, and regularizer, in Figure 14. As can be seen, the cost of batch size and

dimension size increase much when the size increases. But for the number of negative samples, choices of loss functions and regularizers, the influence on cost is not strong as indicated by the average cost.

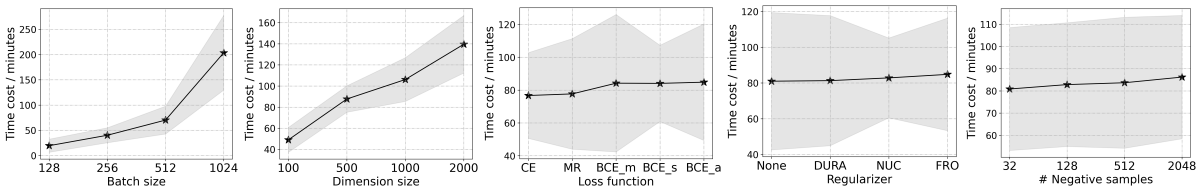

Figure 14: Computing time cost. The dots are the average and the shades are the standard deviation.

C Detail for the search algorithm

We show the reduced and decoupled search space compared with the full space in Table 7. Since the continuous values are not To quantize the ratio of space change after reduction and decoupling, we measure the learning rate and regularization weight in log scale. The size of the whole space $\mathcal{X}$ compared with the decoupled $\hat{\mathcal{X}}$ is

$$3 \times \frac{14}{6} \times \frac{5}{3} \times \frac{5}{3} \times 2 \times 4 \times 5 = 777.8.$$

Hence, the reduced and decoupled space is hundreds times smaller than the full space.

Table 7: The revised HP values in the reduced and decoupled search space compared with the full space.

name	ranges in the whole space	revised ranges
optimizer	{Adam, Adagrad, SGD}	Adam
learning rate	$[10^{-5}, 10^{0}]$	$[10^{-4}, 10^{-1}]$
reg. weight	$[10^{-12}, 10^{2}]$	$[10^{-8}, 10^{-2}]$
dropout rate	[0, 0.5]	[0, 0.3]
inverse relation	{True, False}	{False}
batch size	{128, 256, 512, 1024}	128
dimension size	{100, 200, 500, 1000, 2000}	100

In addition, we show the details for the search procedure by RF+BORE in Algorithm 2.

Algorithm 2 Full procedure of HP search with RF+BORE (in stage one)

Require: KG embedding F, dataset G, search space $\hat{\mathcal{X}}$, budget $B/2$, RF model $y = c(\mathbf{x})$, threshold $\tau = 0.8$.

initialize the RF model and $\mathcal{H} = \emptyset$;
split triplets in G with ratio $9:1$ into G_{tra} and G_{val};
repeat
  randomly sample a set of configurations $\hat{\mathcal{X}}_c \subset \hat{\mathcal{X}}$;
  select $\hat{\mathbf{x}} = \arg\max_{\mathbf{x} \in \hat{\mathcal{X}}_c} y(\mathbf{x})$;
  train embedding model into converge
  $\boldsymbol{P}^* = \arg\min_{\boldsymbol{P}} \mathcal{L}\big(F(\boldsymbol{P}, \hat{\mathbf{x}}), G_{\text{tra}}\big)$;
  evaluate the performance $\hat{y}_{\hat{\mathbf{x}}} = \mathcal{M}\big(F(\boldsymbol{P}^*, \hat{\mathbf{x}}), G_{\text{val}}\big)$;
  record $\mathcal{H} \leftarrow \mathcal{H} \cup \{(\hat{\mathbf{x}}, \hat{y}_{\hat{\mathbf{x}}})\}$;
  % **BORE**:
  set label 0 for configuration in $\mathcal{H}$ with $\hat{y}_{\hat{\mathbf{x}}} < \tau$, and label 1 for $\hat{y}_{\hat{\mathbf{x}}} \geq \tau$;
  update RF model $y = c(\mathbf{x})$ to classify the two labels;
until $B/2$ exhausted.

In Algorithm 1, we increase the batch size and dimension size in stage two. We set the searched range for batch size in stage two as $[512, 1024]$ and dimension size as $[1000, 2000]$. There are some exceptions

due to the memory issues, i.e., dimension size for RESCAL is in $[500, 1000]$; dimension size for TuckER is in $[200, 500]$. For ogbl-wikikg2, since the used GPU only has 24GB memory, we cannot run models with 500 dimensions which requires much more memory in the OGB board. Instead, we set the dimension as 100 to be consistent with the smaller models in OGB board with 100 dimensions, and increase the batch size in $[512, 1024]$ in the second stage.

D Additional experimental results

D.1 Implementation details

Evaluation metrics. We follow (Bordes et al., 2013; Wang et al., 2017; Ruffinelli et al., 2019) to use the filtered ranking-based metrics for evaluation. For each triplet (h, r, t) in the validation or testing set, we take the head prediction $(?, r, t)$ and tail prediction $(h, r, ?)$ as the link prediction task. The filtered rankings on the head and tail are computed as

$$\text{rank}_h = \left|\left\{e \in \mathcal{E} : \big(f(e, r, t) \geq f(h, r, t)\big) \wedge \big((e, r, t) \notin D_{\text{tra}} \cup D_{\text{val}} \cup D_{\text{tst}}\big)\right\}\right| + 1,$$

and

$$\text{rank}_t = \left|\left\{e \in \mathcal{E} : \big(f(h, r, t) \geq f(h, r, e)\big) \wedge \big((h, r, e) \notin D_{\text{tra}} \cup D_{\text{val}} \cup D_{\text{tst}}\big)\right\}\right| + 1,$$

respectively, where $|\cdot|$ is the number of elements in the set. The the two metrics used are:

- Mean reciprocal ranking (MRR): the average of reciprocal of all the obtained rankings.
- Hit@k: the ratio of ranks no larger than k.

For both the metrics, the large value indicates the better performance.

Dataset statistics. We summarize the statistics of different benchmark datasets in Table 8. As shown, ogbl-biokg and ogbl-wikikg2 have much larger size compared with WN18RR and FB15k-237.

Table 8: Statistics of the KG completion datasets.

dataset	#entity	#relation	#train	#validate	#test
WN18RR (Dettmers et al., 2017)	41k	11	87k	3k	3k
FB15k-237 (Toutanova and Chen, 2015)	15k	237	272k	18k	20k
ogbl-biokg (Hu et al., 2020)	94k	51	4,763k	163k	163k
ogbl-wikikg2 (Hu et al., 2020)	2,500k	535	16,109k	429k	598k

Baseline implementation. All the baselines compared in this paper are based on their own original open-source implementations. Here we list the source links:

- Hyperopt (Bergstra et al., 2013), `https://github.com/hyperopt/hyperopt`;
- Ax, `https://github.com/facebook/Ax`;
- SMAC (Hutter et al., 2011), `https://github.com/automl/SMAC3`;
- BORE (Tiao et al., 2021), `https://github.com/ltiao/bore`;
- AutoNE (Tu et al., 2019), `https://github.com/tadpole/AutoNE`.

Searched hyperparameters. We list the searched hyperparameters for each embedding model on the different datasets in Tables 9-12 for reproduction.

Table 9: Searched optimal hyperparameters for the WN18RR dataset.

HP/Model	ComplEx	DistMult	RESCAL	ConvE	TransE	RotatE	TuckER
# negative samples	512	128	128	1VsAll	128	2048	128
loss function	BCE_adv	BCE_adv	BCE_mean	BCE_sum	CE	BCE_adv	CE
gamma	0.00	0.00	0.00	0.00	6.00	3.10	0.00
adv. weight	0.57	1.41	0.00	0.00	0.00	1.93	0.00
regularizer	DURA	NUC	DURA	FRO	FRO	FRO	DURA
reg. weight	$8.64 * 10^{-3}$	$9.58 * 10^{-3}$	$1.76 * 10^{-3}$	$1.00 * 10^{-4}$	$1.00 * 10^{-4}$	$6.51 * 10^{-6}$	$1.42 * 10^{-3}$
dropout rate	0.25	0.29	0.00	0.00	0.20	0.00	0.00
optimizer	Adam	Adam	Adam	Adam	Adam	Adam	Adam
learning rate	$1.77 * 10^{-3}$	$4.58 * 10^{-3}$	$1.73 * 10^{-3}$	$1.00 * 10^{-3}$	$1.00 * 10^{-3}$	$6.43 * 10^{-4}$	$1.37 * 10^{-3}$
initializer	xavier_norm	norm	uniform	uniform	uniform	norm	uniform
batch size	512	1024	512	1024	512	512	512
dimension size	1000	2000	1000	2000	1000	1000	200
inverse relation	False	False	False	False	False	False	False

Table 10: Searched optimal hyperparameters for the FB15k-237 dataset.

HP/Model	ComplEx	DistMult	RESCAL	ConvE	TransE	RotatE	TuckER
# negative samples	512	kVsAll	2048	512	512	2048	2048
loss function	BCE_adv	CE	CE	BCE_sum	BCE_adv	BCE_adv	BCE_adv
gamma	0.00	0.00	0.00	0.00	6.76	7.58	0.00
adv. weight	1.93	0.00	0.00	0.00	1.99	1.57	1.94
regularizer	DURA	FRO	DURA	DURA	FRO	DURA	DURA
reg. weight	$9.75 * 10^{-3}$	$1.00 * 10^{-4}$	$9.01 * 10^{-3}$	$6.42 * 10^{-3}$	$2.16 * 10^{-3}$	$5.12 * 10^{-3}$	$1.47 * 10^{-4}$
dropout rate	0.22	0.30	0.00	0.08	0.03	0.02	0.02
optimizer	Adam	Adam	Adam	Adam	Adam	Adam	Adam
learning rate	$9.70 * 10^{-4}$	$1.00 * 10^{-3}$	$1.19 * 10^{-3}$	$2.09 * 10^{-3}$	$2.66 * 10^{-4}$	$2.98 * 10^{-4}$	$3.19 * 10^{-4}$
initializer	uniform	normal	xavier_norm	normal	xavier_norm	uniform	normal
batch size	1024	1024	512	1024	512	512	512
dimension size	2000	2000	500	500	1000	1000	500
inverse relation	False	False	False	False	False	False	False

Table 11: Searched optimal hyperparameters for the ogbl-biokg dataset.

HP/Model	ComplEx	DistMult	TransE	RotatE
# negative samples	512	512	128	128
loss function	CE	CE	CE	BCE_adv
gamma	0.00	0.00	7.60	18.24
adv. weight	0.00	0.00	0.00	1.94
regularizer	NUC	NUC	NUC	DURA
reg. weight	$1.38 * 10^{-3}$	$1.20 * 10^{-6}$	$6.99 * 10^{-3}$	$1.09 * 10^{-8}$
dropout rate	0.01	0.00	0.00	0.00
optimizer	Adam	Adam	Adam	Adam
learning rate	$1.89 * 10^{-3}$	$1.25 * 10^{-3}$	$1.24 * 10^{-4}$	$1.11 * 10^{-4}$
initializer	uniform	xavier_norm	xavier_norm	normal
batch size	1024	1024	1024	1024
dimension size	2000	2000	2000	2000
inverse relation	False	False	False	False

Table 12: Searched optimal hyperparameters for the ogbl-wikikg2 dataset

HP/Model	ComplEx	DistMult	TransE	RotatE
# negative samples	32	32	128	32
loss function	CE	CE	CE	BCE_mean
gamma	0.00	0.00	9.41	12.00
adv. weight	0.00	0.00	0.00	0.00
regularizer	DURA	DURA	DURA	NUC
reg. weight	$9.58 * 10^{-7}$	$2.43 * 10^{-8}$	$2.29 * 10^{-3}$	$7.15 * 10^{-4}$
dropout rate	0.00	0.00	0.01	0.25
optimizer	Adam	Adam	Adam	Adam
learning rate	$1.34 * 10^{-4}$	$1.98 * 10^{-4}$	$6.44 * 10^{-4}$	$1.13 * 10^{-5}$
initializer	xavier_norm	xavier_norm	xavier_norm	normal
batch size	1024	1024	1024	1024
dimension size	100	100	100	100
inverse relation	False	False	False	False

D.2 Results on general benchmarks

We compare the types of results on WN18RR and FB15k-237 in Table 13. In the first part, we show the results reported in the original papers. In the second part, we show the reproduced results in (Ruffinelli et al., 2019). And in the third part, we show the results of the HPs searched by TOSS.

*Table 13: Performance on WN18RR and FB15k-237 dataset. The **bold numbers** mean the best performances of the same model, and the underlines mean the second best.*

		WN18RR				FB15k-237			
		MRR	Hit@1	Hit@3	Hit@10	MRR	Hit@1	Hit@3	Hit@10
Original	ComplEx	0.440	0.410	0.460	0.510	0.247	0.158	0.275	0.428
	DistMult	0.430	0.390	0.440	0.490	0.241	0.155	0.263	0.419
	RESCAL	0.420	-	-	0.447	0.270	-	-	0.427
	ConvE	0.430	0.400	0.440	**0.520**	0.325	0.237	0.356	0.501
	TransE	0.226	-	-	0.501	0.294	-	-	0.465
	RotatE	0.476	**0.428**	0.492	0.571	0.338	0.241	**0.375**	**0.533**
	TuckER	0.470	**0.443**	0.482	0.526	**0.358**	**0.266**	**0.394**	**0.544**
LibKGE (Ruffinelli et al., 2019)	ComplEx	0.475	0.438	0.490	0.547	0.348	0.253	0.384	**0.536**
	DistMult	0.452	**0.413**	0.466	0.530	0.343	0.250	**0.378**	**0.531**
	RESCAL	0.467	**0.439**	0.480	0.517	0.356	0.263	0.393	**0.541**
	ConvE	**0.442**	**0.411**	**0.451**	0.504	**0.339**	**0.248**	**0.369**	0.521
	TransE	0.228	**0.053**	0.368	0.520	0.313	0.221	0.347	0.497
TOSS (ours)	ComplEx	**0.483**	**0.439**	**0.501**	**0.564**	**0.355**	**0.266**	**0.389**	0.533
	DistMult	**0.453**	0.406	**0.468**	**0.545**	**0.344**	**0.253**	0.377	0.525
	RESCAL	**0.478**	0.434	**0.499**	**0.559**	**0.359**	**0.272**	**0.395**	0.532
	ConvE	0.435	0.405	0.444	0.500	0.330	0.237	0.362	**0.522**
	TransE	**0.232**	0.033	**0.394**	**0.540**	**0.328**	**0.229**	**0.369**	**0.523**
	RotatE	**0.479**	0.426	**0.499**	**0.585**	**0.339**	**0.246**	0.372	0.527
	TuckER	**0.480**	0.437	**0.501**	**0.556**	0.347	0.255	0.382	0.535

D.3 Full results for OGB

Table 14: Full results on ogbl-biokg and ogbl-wikikg2 dataset.

		ogbl-biokg			ogbl-wikikg2		
		Test MRR	Val MRR	#parameters	Test MRR	Val MRR	#parameters
OGB board	ComplEx	0.8095±0.0007	0.8105±0.0001	187,648,000	0.4027±0.0027	0.3759±0.0016	1,250,569,500
	DistMult	0.8043±0.0003	0.8055±0.0003	187,648,000	0.3729±0.0045	0.3506±0.0042	1,250,569,500
	RotatE	0.7989±0.0004	0.7997±0.0002	187,597,000	0.2530±0.0034	0.2250±0.0035	250,087,150
	TransE	0.7452±0.0004	0.7456±0.0003	187,648,000	0.4256±0.0030	0.4272±0.0030	1,250,569,500
TOSS	ComplEx	0.8383±0.0006	0.8394±0.0003	187,648,000	0.4898±0.0017	0.5098±0.0023	250,113,900
	DistMult	0.8254±0.0003	0.8261±0.0004	187,648,000	0.4866±0.0078	0.4921±0.0075	250,113,900
	RotatE	0.8018±0.0005	0.8028±0.0003	187,597,000	0.2845±0.0026	0.2604±0.0034	250,087,150
	TransE	0.7771±0.0003	0.7778±0.0003	187,648,000	0.4745±0.0021	0.4955±0.0013	250,113,900